Chemistry and Materials

The Center for Science Innovation

Research Article

Chem. Mater. 3 (3) 2024, 80-89

Electrodeposition of Thin Film Cu-Zn-Sn Alloy for Water Splitting Application

Reinardo Ramawijaya Widakusuma[1,*], Fathir Azzaki Iradata[1], Mokhamad Ali Rizqi Maulana[2], Ikhwan Nur Rahman[3]

[1]Department of Chemistry, Faculty of Mathematics and Natural Science, Universitas Negeri Jakarta, Jl. Rawamangun Muka, Jakarta 13220, Indonesia

[2]The Center for Science Innovation, Jakarta 13120, Indonesia

[3]Department of Physics, Research Institute for Nanoscale Science and Technology, Chungbuk National University, Chungdae-ro, Seowon-gu, Cheongju, Chungcheongbuk-do 28644, Republic of Korea

*Corresponding author: reinardorw7977@gmail.com

Received
2 September 2024

Received in revised form
10 October 2024

Accepted
11 October 2024

Published online
31 October 2024

DOI
https://doi.org/10.56425/cma.v3i3.82

Abstract

An energy transition to renewable energy sources is necessary due to the scarcity of fossil fuels and their detrimental effects on the environment. Water splitting process is one of the practical and effective way that does not occur spontaneously. This study investigates catalytic activity of Cu-Zn-Sn (CZT) photocatalyst in hydrogen evolution and oxygen evolution reaction. The CZT deposited with varied electrolyte's pH of 6 and 9 on indium tin oxide substrate at the room temperature for 600 seconds. According to the X-ray diffraction patterns, there were Cu_6Sn_5, Cu_5Zn_8, and Sn metal phases with monoclinic, cubic, and cubic crystal systems. The scanning electron microscopy technique results of all CZT alloy sample showed a dense, non-uniform, and polycrystalline surface structure. The CZT alloys were found to have an average particle size of 0.35 µm. CZT alloys can produce a photocurrent density of 0.19 mA/cm² at a potential of 1.29 V vs RHE. the charge transfer resistance of CZT synthesized at pH 6 is lower (21.48 Ω) compared to pH 9 (28.36 Ω). The Tafel slope of HER for pH 9 CZT was -133 mV/dec, which was lower than that of pH 6 CZT (-88 mV/dec), indicating faster H_2 production and corrosion resistance on pH 9 CZT.

Keywords: electrodeposition, CZT alloy, water splitting

1. Introduction

The transition to renewable energy sources is necessary due to the scarcity of fossil fuels and their negative effects on the environment. Solar power is a clean and renewable energy source, but it has limitations, including low portability, significant temporal and seasonal variability, and low energy density. To address these challenges, photocatalysis is employed to convert solar radiation into chemical energy that can be stored in the form of efficient and clean hydrogen energy [1,2].

One practical and effective way to achieve storable hydrogen with lessening extreme energy shortages and greenhouse gas emissions is by photoelectrochemical water-splitting [3]. This process relies on semiconductor-based materials to convert solar radiation into chemical energy [4]. To initiate the redox reactions necessary for water splitting, the semiconductor-based photocatalyst must have a minimum band gap of 1.23 eV [5].

One of the very popular light-absorbing materials with suitable band gaps for water splitting is Cu-Zn-Sn/S (CZTS). CZTS is a compound with a kesterite crystal structure and a direct E_{gap} of 1.5 eV and a conduction band (CB) edge potential of - 0.7 V vs reversible hydrogen electrode (RHE). CZTS is an appealing example of a p-type quaternary semiconductor [6]. The benefits of CZTS include its fair absorption characteristics, environmental friendliness, and abundance of materials found in the earth's crust, making it a good option for a photocathode [7–9]. However, the

sulfurization process in the production of CZTS films requires high temperatures and often involves the use of toxic H_2S gas, furthermore increasing costs and posing significant health risks [10–12]. Therefore, it is essential to explore alternative methods for producing Cu-Zn-Sn (CZT) films to avoid the sulfurization process, thereby reducing costs and eliminating the associated health and environmental hazards.

Electrochemical deposition is one of the most appealing non-vacuum growth methods due to its relatively low equipment costs, ease of use in industry on large substrates, and ability to prepare electrolytes from inexpensive, low-cost precursors like Cu, Zn, Sn, Co, Fe, and Ni salts [6,13–15]. However, the resulting materials often exhibit low efficiency in photocatalytic activity [16].

The low efficiency of the photocatalyst is influenced by the surface phase dependence of the photocatalytic activity [17,18]. The accessible surface for analyte adsorption and photocatalytic reactions is decreased by aggregation. Furthermore, big aggregates (diameter <1 µm) cause interior crystals to be shaded from incoming photons, which results in fewer excitation events and decreased photocatalytic activity [19]. To enhance the photocatalytic activity of CZT, the crystal structure and morphology of the catalyst can be modified to improve the charge transfer of electrons [20].

To achieve this, there are factors that can alter the deposition conditions: type of substrate (FTO, Mo-coated glass) [21], type of electrodeposition (sequential electrodeposition, co-electrodeposition, or single-step electrodeposition) [22,23], use of forced convection (stirring) during electrodeposition, electrolyte composition, pH, and deposition time [15,24,25]. This deposition condition must therefore be tailored to a particular set of parameters. Previous study shows the pH of the electrolyte in range 4-5 resulted in the growth of non-uniform and rough films, while in range 6-8 yielded dense and smooth films. This indicated a significant influence on the morphology of co-deposited CZT metal precursor films. This investigation of electrolyte pH and morphological differences may have an impact on the evolution of hydrogen [26].

In a related study, it was observed that the electrodeposition of CZT alloys with an excess $SnCl_2$ concentration resulted in a notable alteration in the surface morphology, characterized by the formation of significantly larger particle sizes [27]. This highlights the potential for morphology regulation through concentration parameters, particularly in the case of $SnCl_2$ during electrodeposition.

In this study, CZT was deposited with varied electrolytes's pHs of 6 and 9 to analyze its impact on hydrogen and oxygen evolution. To synthesize CZT films with the desired composition are electrodeposited on ITO substrate at room temperature for 600 seconds. Furthermore, the structural, morphological, compositional, and photoelectrochemical characteristics of the electrodeposited CZT are examined.

2. Materials and Method

2.1 Materials

All chemicals, including $CuSO_4.5H_2O$, $ZnSO_4.7H_2O$, $SnCl_2$, $Na_3C_6H_5O_7.2H_2O$, NaOH, KOH, Na_2SO_4, and C_2H_5OH, were procured from PT Merck Indonesia. The chemicals were used as received without any further purification.

2.2 Synthesis of CZT alloy

The electrodeposition of CZT alloys was conducted in a three-electrode cell configuration, utilizing a platinum wire as the counter electrode, an Ag/AgCl reference electrode (KCl 3 M solution), and an indium tin oxide (ITO) as the working electrode. The substrates were subjected to a cleansing process involving the use of ethanol and distilled water, with the objective of eliminating any residual contaminants. Subsequently, the substrate was wait until dry.

The precursor solution was prepared in a volume of 25 ml and consisted of 0.02 M $CuSO_4.5H_2O$, 0.01 M $ZnSO_4.7H_2O$, 0.02 M $SnCl_2$, and 0.2 M $Na_3C_6H_5O_7.2H_2O$ as complexing agents. The precursor solution was adjusted to pH 6 and 9 using 10 M NaOH and placed in the chamber with the working electrode ITO, counter electrode Platinum, and reference electrode Ag/AgCl. Subsequently, electrodeposition was conducted with a potential of -1.23 V vs Ag/AgCl (KCl 3 M) for a duration of 600 seconds at room temperature.

2.3 Characterization

The surface morphology and elemental composition were analyzed using a scanning electron microscope (SEM) coupled with an energy-dispersive X-ray spectrometer (EDS). The structure and phase were analyzed using Panalytical AERIS X-ray diffractometer (XRD).

2.4 Photoelectrochemical analysis

Photoelectrochemical analysis of CZT thin films was performed by photoelectrochemical (PEC) and electrochemical impedance spectroscopy (EIS) techniques. Hydrogen evolution reaction (HER) and oxygen evolution reaction (OER) activity were tested to determine the overpotential and stability of CZT thin films. The

measurements were performed in a 0.5 M Na_2SO_4 electrolyte and were controlled by a Corrtest C310 workstation in a quartz three-electrode cell with a platinum wire serving as the counter electrode and Ag/AgCl (KCl 3 M) as the reference electrode. Photoelectrochemical measurements were conducted using a solar simulator with a halogen lamp AM 1.5 G-calibrated. EIS measurements were performed in the frequency region of 100 kHz to 0.1 Hz with an amplitude of 10 mV under light irradiation. Linear sweep voltammetry (LSV) was employed to record photocurrents under bias potentials between 0.1 V to 1.9 V vs RHE. The HER test was conducted over a potential range of -0.6 V to 0 V vs RHE, while the OER was performed over a range of 1.3 V to 2.5 V vs RHE, with a scan rate of 50 mV/s in an electrolyte solution of 25 mL of 0.5 M KOH. All the measured potentials were carried out and converted with respect to the reversible hydrogen electrode (equation 1).

$$E_{(RHE)} = E_{(Ag/AgCl)} + 0.6106\ V\ (in\ 0.5\ Na_2SO_4) \quad (1)$$

3. Results and Discussion

3.1 Morphology, composition, and structure analysis

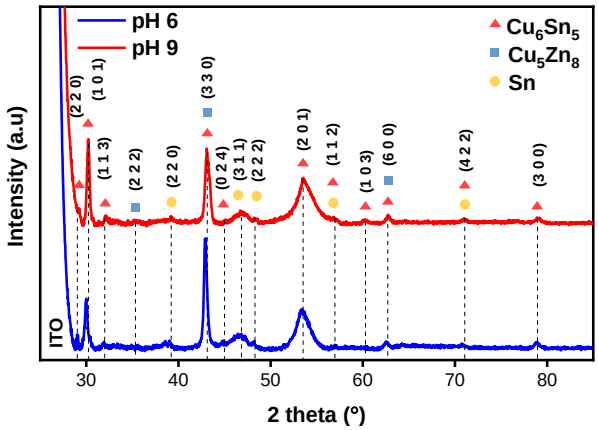

Figure 1. XRD pattern of CZT alloys synthesized at pH 6 and pH 9.

The Cu-Zn-Sn (CZT) alloys that have been deposited on the ITO substrate were then characterized. The XRD patterns of CZT alloys samples are shown in Fig. 1. The synthesis of the CZT alloy results in the formation of three different phases: Cu_5Zn_8, Cu_6Sn_5, and Sn metal [27,28]. The XRD pattern shows that the Cu_5Zn_8 phase is identified by the presence of peaks at 2θ = 35.14°, 43.39°, and 62.99°, which match the ICDD standard data card # 00-025-1228. This phase possesses a cubic crystal structure. The Cu_6Sn_5 phase has peaks at 2θ = 29.09°, 30.17°, 32.04°, 43.39°, 44.89°, 53.58°, 56.96°, 60.28°, 62.99°, 71.12°, and 78.90°, which conform to the ICDD standard data card # 00-047-1575 and indicate a monoclinic crystal structure. Furthermore, the Sn phase is generated, which is distinguished by the emergence of peaks at 2θ = 39.24°, 46.69°, 48.37°, 56.96°, and 71.12°. These peaks align with the ICDD standard data card No. 03-065-0298, indicating a cubic crystal system.

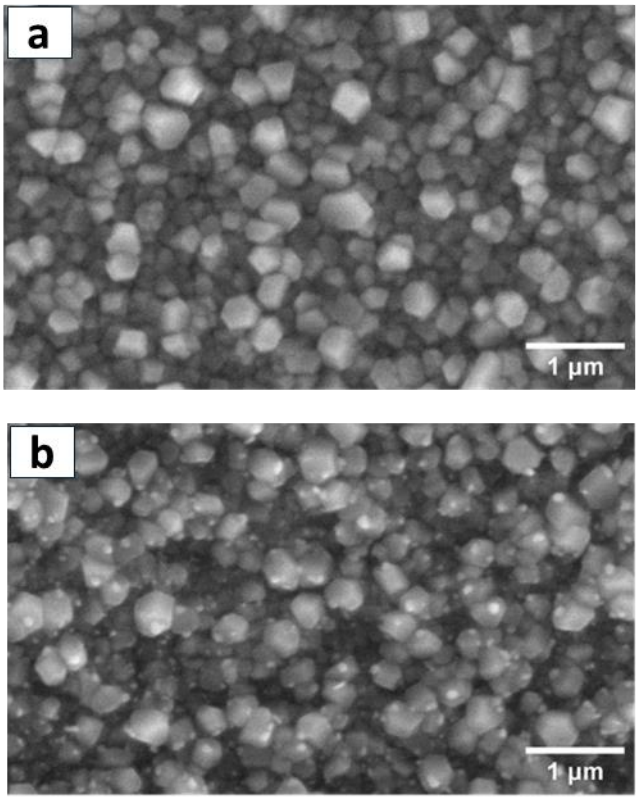

Figure 2. SEM images of CZT alloys synthesized at (a) pH 6 and (b) pH 9.

Modifying the pH from 6 to 9 in the XRD pattern resulted in the emergence of a plane Cu_6Sn_5 crystal in the (1 0 3) plane at 2θ = 60.28°. This phenomenon is likely attributable to the influence of the OH^- ion concentration on the conditions governing crystal growth, which has resulted in the growth of Cu_6Sn_5 with a specific orientation. At higher pH values, such as pH 9, the formation of this peak is more pronounced, thereby underscoring the influence of elevated pH on the orientation of crystal growth [29].

Fig. 2 shows the top view of the CZT alloys thin film, which was analyzed using a SEM. The results of the CZT alloys revealed the presence of compact, non-uniform, and polycrystalline surface structures in all samples. The particle morphology exhibited monoclinic, cubic, and spherical forms, corresponding to the Cu_5Zn_8, Cu_6Sn_5, and Sn phases, respectively. This variation in morphology indicates the presence of different phases in the alloy. The average particle size was approximately 350 nm, but at a pH of 9, smaller clusters below 90 nm were observed, likely

due to the enhanced reactivity of Zn in alkaline conditions, promoting the formation of finer Cu_5Zn_8 particles.

The detection of distinct phases, such as Cu_6Sn_5 and Cu_5Zn_8, in the XRD pattern may exhibit peak overlap due to similar lattice parameters. Furthermore, the absence of a full CZT alloy phase may be attributed to low intensities or overlapping peaks, with monometallic Sn appearing in weaker intensities. The presence of such phases indicates that Zn deposition becomes more pronounced at higher pH, which aligns with the changes in particle size and distribution observed in the SEM analysis.

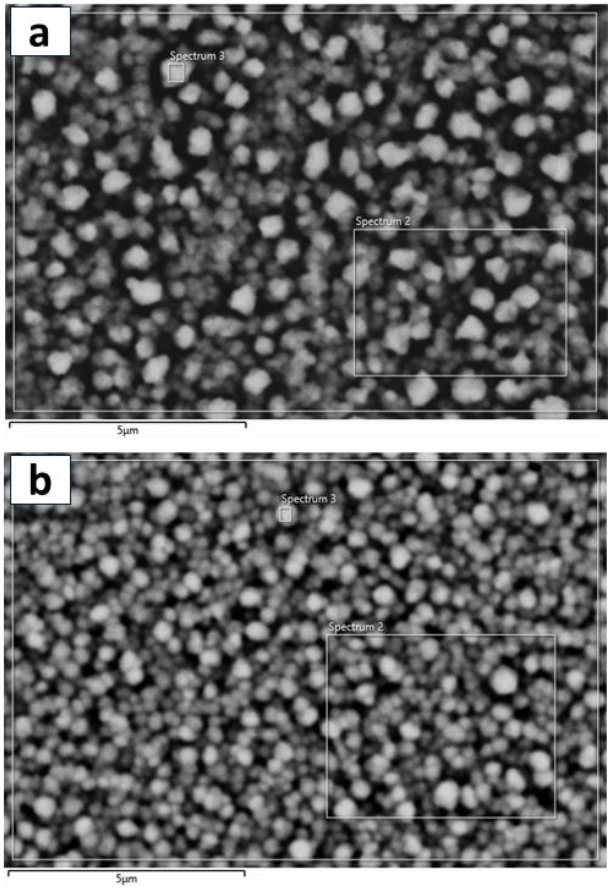

Figure 3. SEM-EDS imaging region of CZT alloys synthesized at (a) pH 6 and (b) pH 9.

The results of the EDS analysis of the CZT thin film are presented in Fig. 3. The figure illustrates the scanning region of the elemental composition of Cu, Zn, and Sn present in the sample. As indicated by the EDS findings, modifying the solution pH from 6 to 9 during the electrodeposition of the CZT alloy has the effect of increasing the concentration of Zn, as illustrated in Table 1.

The relatively high zinc content in comparison to the results at pH 6 (zinc content of only 0.62%) indicates that pH 9 conditions are more conductive to the precipitation of significant amounts of zinc. At this composition, a considerable amount of Zn is involved in the formation of Zn-rich phases, with one such candidate phase being Cu_5Zn_8, which stoichiometrically contains approximately 38-45% Zn in its alloy [30,31].

In CZT alloys, a change in pH from 6 to 9 has been observed to result in a change in morphology on a micrometer scale. CZT alloys synthesized at pH 6 will form larger grains of particles with a coarse and uneven composition, as evidenced by the difference in color between light and dark particles. In contrast, at pH 9, the formation of smaller grains, agglomerates, and a more even composition is evident.

In a previous study, Farbod et. al. [32] proposed that Cu_5Zn_8 nanoparticles can be attracted to larger particles, and that the grain growth of Cu_5Zn_8 depends on grain boundaries motion. In CZT alloy, it was found that the effect of pH 9 can form the Cu_5Zn_8 phase, which is characterized by white dots in SEM results.

Table 1. Average chemical compositions of CZT alloys synthesized at pH 6 and pH 9.

Spectrum 1				
Element	pH 6		pH 9	
	Weight %	**Atomic %**	**Weight %**	**Atomic %**
Cu	42.32	57.56	40.15	50.12
Zn	0.76	1.00	14.54	18.00
Sn	56.92	41.44	45.30	34.43
Total	100.00	100.00	100.00	100.00

Spectrum 2				
Element	pH 6		pH 9	
	Weight %	**Atomic %**	**Weight %**	**Atomic %**
Cu	42.43	57.72	40.35	51.36
Zn	0.60	0.79	14.39	17.80
Sn	56.97	41.49	45.26	30.84
Total	100.00	100.00	100.00	100.00

Spectrum 3				
Element	pH 6		pH 9	
	Weight %	**Atomic %**	**Weight %**	**Atomic %**
Cu	35.09	50.10	38.59	50.29
Zn	0.45	0.62	12.07	15.29
Sn	64.47	49.28	49.35	34.42
Total	100.00	100.00	100.00	100.00

3.2 Photoelectrochemical analysis

The CZT alloys synthesized at a pH of 6 were subjected to PEC testing utilizing LSV technique to quantify the photocurrent density Fig. 4. The CZT alloys was evaluated throughout a potential range of 0.1 V to 1.9 V compared to the RHE using a solar simulator. The CZT alloys exhibit a photocurrent density of 0.19 mA/cm^2 when subjected to a potential of 1.29 V vs RHE.

The morphology of CZT alloys is a combination of cubic and monoclinic crystal systems. Materials with higher symmetry, such as the cubic structure in Cu_5Zn_8 and Sn

phases, generally exhibit higher carrier mobility due to reduced scattering of charge carriers by lattice vibrations and impurities [33]. The absence of defects such as impurities, vacancies, or dislocations in CZT alloys can act as scattering center, thereby reducing carrier mobility. Lower defect density is associated with higher carrier mobility, which is important for efficient charge transport within the material. CZT alloys with high mobility can achieve higher photocurrent densities because more charge carriers are effectively transported to the electrode [34].

A particle size of 350 nm can increase the surface area of the material, which increasing the number of active sites available for catalytic reactions. This increase in surface area can lead to a higher photocurrent density as more sites are available for electron transfer. Larger particle sizes can increase the thickness of the thin film, which can reduce the photocurrent density [35].

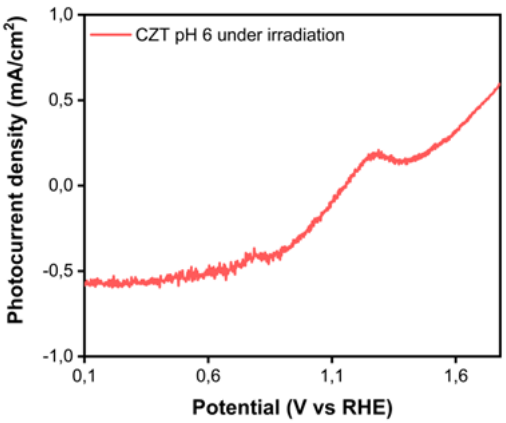

Figure 4. Photocurrent response under irradiation measured from CZT synthesized at pH 6 over a potential range of 0.1 V to 1.9 V vs RHE with scan rate at 50 mV/s in 0.5 M Na_2SO_4 solution.

3.3 Electrochemical impedance spectroscopy analysis

EIS was used to measure the impedance response of the CZT alloys. The CZT alloys was measured at ambient temperature in a 0.5 M Na_2SO_4 electrolyte solution under light irradiation. According to the data in Table 2, the difference in R_{ct} and R_s values is not significant, considering that the average particle size of CZT alloys is 350 nm. With a larger surface area, more active sites are available for electrochemical reactions, which can lower the R_{ct} value. This is because charge transfer becomes more efficient when more sites are available for interaction between the electrode and the electrolyte.

The formation of the Cu_6Sn_5 phase in CZT alloys, commonly referred to as tin bronze, is significant due to its protective oxide layer, which effectively prevents corrosion. This protective layer enhances the stability and functionality of the electrocatalyst over time. A well-formed oxide layer is crucial as it facilitates improved charge transfer between the electrode and electrolyte, ensuring efficient electron transfer necessary for successful water splitting reactions [36].

Table 2. R_{ct} and R_s values of CZT synthesized at pH 6 and 9.

CZT	R_{ct}	R_s
pH 6	22.37 Ω	9.14 Ω
pH 9	28.36 Ω	10.63 Ω

In addition, the presence of the Cu_5Zn_8 phase contributes to the electrochemical activity of the alloy. The higher zinc content in this phase results in increased reactivity compared to copper, which can elevate corrosion rates and oxidation reactions. This heightened reactivity influences the electrochemical impedance, often leading to higher charge transfer resistance (R_{ct}) values.

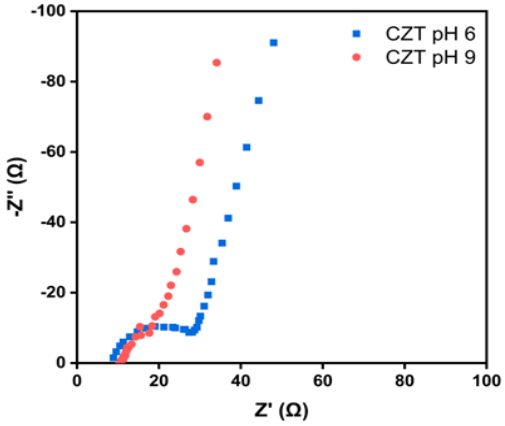

Figure 5. Nyquist plots measured by simulated solar irradiation for CZT synthesized at different pH in 0.5 M Na_2SO_4 solution.

When comparing the alloys synthesized at different pH levels, the CZT alloy at pH 6 exhibits a more homogeneous structure with larger, more regular grain sizes, facilitating efficient charge transfer and resulting in lower R_{ct} values. Conversely, the CZT alloy produced at pH 9 displays a morphology with smaller grains and white dots on larger particles, leading to an inhomogeneous structure that increases charge transfer resistance. This necessitates longer electron transfer times at the interface, culminating in higher R_{ct} values than those observed for the pH 6 alloy. Thus, while the smaller particles formed at pH 9 may suggest potential for enhanced catalytic performance, the irregular structure ultimately hampers efficient charge transfer, highlighting the complex interplay between surface morphology and electrochemical activity [37].

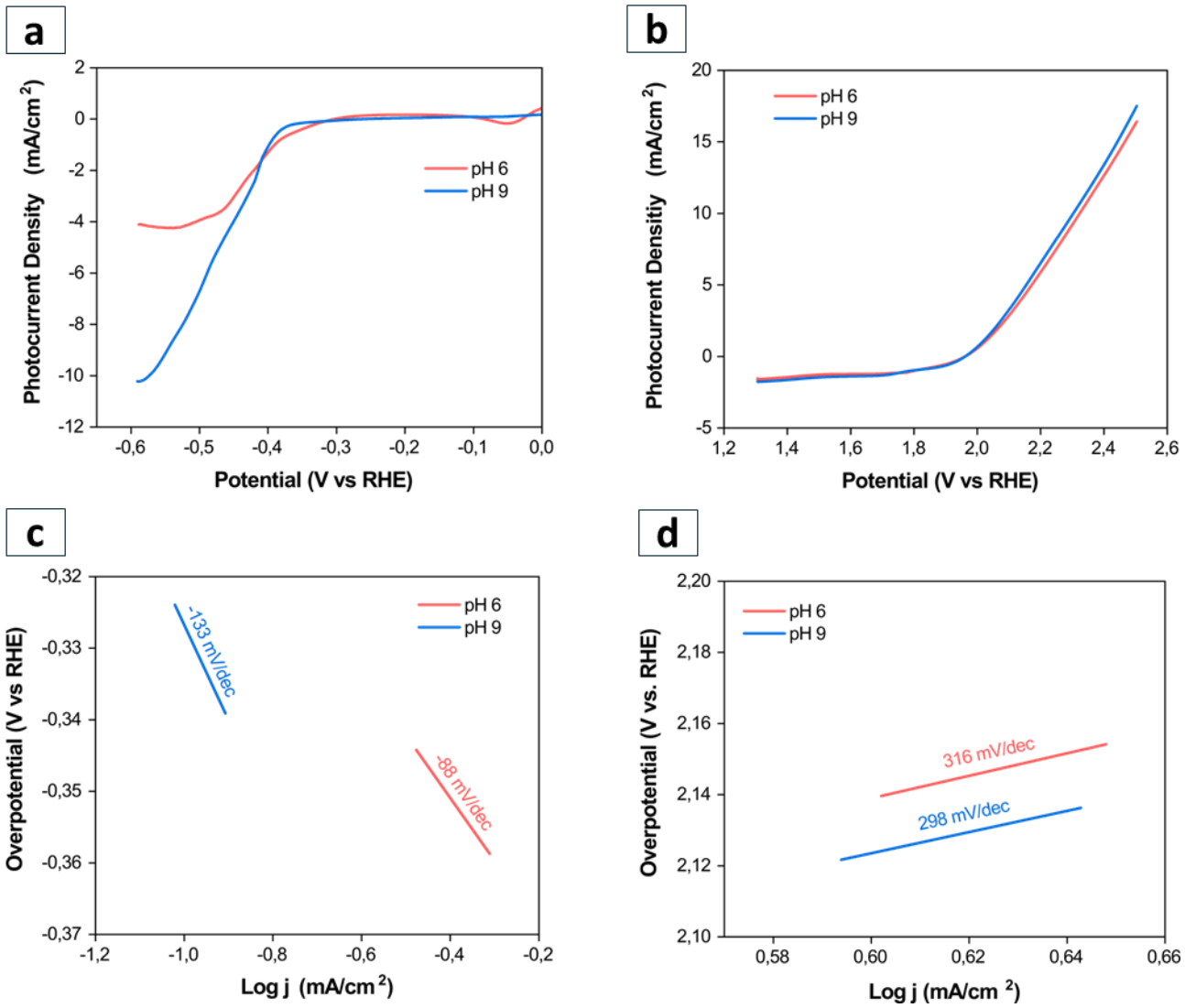

Figure 6. LSV curves of (a) OER and (b) OER of CZT alloys testing. The OER and HER tests were conducted in 0.5 M KOH electrolyte with a scan rate of 50 mV/s. Tafel Slope of (c) HER and (d) OER of CZT alloys under solar simulator irradiation.

3.4 HER and OER activities

The LSV curves for both samples provide crucial insights into the performance of the CZT catalysts in the HER and OER in Fig. 6. shows HER at pH 9, the catalyst displays a lower overpotential at 10 mA in comparison to the pH 6 sample, signifying superior catalytic performance. The increasing presence of zinc enhances the reaction kinetics of the HER due to its higher reactivity, which allows for more effective electron transfer [38]. When a voltage is applied, protons in the electrolyte migrate toward the negatively charged electrode CZT, where they are attracted to the available active sites. Upon reaching these sites, the protons accept electrons supplied by the conductive properties of the CZT alloy, leading to the formation of hydrogen gas. The efficiency of the HER is further improved by the favorable morphology of the CZT alloy, which provides a larger surface area and more active sites for the reaction to occur. This suggests that the CZT alloy synthesized at pH 9 requires less energy to drive the hydrogen evolution reaction, making it a more efficient catalyst under these conditions. Similarly, in the OER, the overpotential at 10 mA for the pH 9 sample is also slightly lower than that of the pH 6 sample, reinforcing the superior performance of the pH 9 catalyst in facilitating oxygen evolution. The OER involves the oxidation of water molecules to form oxygen gas, protons, and electrons. This reaction occurs at the anode of the electrochemical cell, where the CZT catalyst facilitates the transfer of electrons from the water molecules to the CB of the CZT. The rate of this reaction is influenced by the presence of metal oxides, particularly the Cu_6Sn_5 phase in CZT, which forms a protective oxide layer. This layer enhances charge transfer and stability, allowing the reaction to proceed more

efficiently while minimizing corrosion and degradation of the catalyst.

Despite the higher charge transfer resistance R_{ct} observed at pH 9, the increased surface area and active sites boost the reaction kinetics, ultimately leading to better catalytic performance in both the HER and OER. Therefore, the overall performance of the catalyst at pH 9 is superior, driven by the improved morphology and active site availability, which outweigh the influence of higher R_{ct}.

The tafel slope can be introduced as a critical parameter for analyzing the reaction kinetics of the catalysts. The Tafel slope, which is found by plotting the log current density (j) against the iR-corrected overpotential (η), shows how well the catalyst changes the overpotential into current. It links the rate of the reaction to the overpotential, which is the applied potential that is higher than the equilibrium potential to start the reaction and free the substance at the electrodes [39]. The equation is typically expressed in the logarithmic form [40]:

$$\eta = a + b\ log(j).$$

The HER and OER obtained using the pH 9 CZT sample demonstrates superior performance compared to the pH 6 sample. In the HER analysis, the pH 9 CZT exhibits a lower Tafel slope of -133 mV/dec, indicating faster hydrogen production and more favorable reaction kinetics than the pH 6 CZT, which has a Tafel slope of -88 mV/dec. This enhanced performance is likely due to the pH 9 condition providing more active sites for the reaction. Similarly, for the OER, the pH 9 CZT sample outperforms the pH 6 sample with a Tafel slope of 298 mV/dec versus 316 mV/dec. The lower Tafel slope at pH 9 reflects better reaction kinetics and a higher current density with less overpotential, highlighting the increased catalytic activity of the pH 9 sample in facilitating the oxygen evolution reaction [41].

The corrosion potentials and corrosion currents are parameters that can determine the stability of the catalyst for the water splitting application. This corrosion parameter calculated from Tafel plots is shown in Table 3. The CZT synthesized in pH 9 has better corrosion resistance and stability than the CZT synthesized in pH 6 due to its smaller i_{corr} value. This corrosion parameter can determine the stability of the catalyst for the water splitting application.

Table 3. The corrosion potentials (E_{corr}) and corrosion currents (i_{corr}) of CZT alloys synthesized at pH 6 and 9.

pH of CZT	HER		OER	
	E_{corr} (V)	i_{corr} (mA)	E_{corr} (V)	i_{corr} (mA)
6	-1.31	-0.93	2,01	-0,91
9	-1.27	-1.58	2,02	-1,01

4. Conclusion

CZT alloys thin films were successfully synthesized using the electrodeposition method on an ITO substrate. The synthesis of CZT alloys at different pH levels significantly impacts their surface morphology, which in turn affects their electrochemical performance. The CZT alloy synthesized at pH 6 exhibits a more homogeneous surface morphology characterized by larger (350 nm), well-defined grains that facilitate efficient charge transfer and result in lower R_{ct} values. This regularity in grain size allows for smoother electron flow between the electrode and the electrolyte, enhancing overall efficiency. Conversely, the alloy produced at pH 9 features a less uniform morphology with smaller particle sizes (90 nm) and irregular clusters, which increase the surface area and create more active sites for reactions. Although this morphology improves catalytic performance for HER and OER, it also leads to higher R_{ct} due to increased resistance from the inhomogeneous structure. Thus, while the smaller particles at pH 9 provide advantages in terms of catalytic activity, they complicate charge transfer efficiency, illustrating the intricate interplay between surface morphology and electrochemical behavior in CZT alloys.

Acknowledgement

The authors thank The Center for Science Innovation supported this study by providing all materials, electrochemical workstation and funding for characterization.

References

[1] C. Bie, L. Wang, J. Yu, Challenges for photocatalytic overall water splitting, *Chem*. **8** (2022). https://doi.org/10.1016/j.chempr.2022.04.013.

[2] Chika Shafa Maura, Muhammad Fathar Aulia, Raudhatul Hadawiyah, Wulan Kharisma Dera, Hilman Syafei, Synthesis of CoNi by Electrodeposition Technique and its Application as an Electrocatalyst for Water Splitting, *Chemistry and Materials*. **2** (2023). https://doi.org/10.56425/cma.v2i3.64.

[3] B. Zhang, Y. Zheng, T. Ma, C. Yang, Y. Peng, Z. Zhou, M. Zhou, S. Li, Y. Wang, C. Cheng, Designing MOF Nanoarchitectures for Electrochemical Water Splitting, *Advanced Materials*. **33** (2021). https://doi.org/10.1002/adma.202006042.

[4] S.K. Saraswat, D.D. Rodene, R.B. Gupta, Recent advancements in semiconductor materials for photoelectrochemical water splitting for hydrogen production using visible light, *Renewable and*

Sustainable Energy Reviews. **89** (2018). https://doi.org/10.1016/j.rser.2018.03.063.

[5] T. Jafari, E. Moharreri, A.S. Amin, R. Miao, W. Song, S.L. Suib, Photocatalytic water splitting - The untamed dream: A review of recent advances, *Molecules*. **21** (2016). https://doi.org/10.3390/molecules21070900.

[6] R. Kondrotas, R. Juškenas, A. Naujokaitis, A. Selskis, R. Giraitis, Z. Mockus, S. Kanapeckaite, G. Niaura, H. Xie, Y. Sánchez, E. Saucedo, Characterization of Cu2ZnSnSe4 solar cells prepared from electrochemically co-deposited Cu-Zn-Sn alloy, *Solar Energy Materials and Solar Cells*. **132** (2015). https://doi.org/10.1016/j.solmat.2014.08.010.

[7] R.J. Deokate, R.S. Kate, S.C. Bulakhe, Physical and optical properties of sprayed Cu 2 ZnSnS 4 (CZTS) thin film: effect of Cu concentration, *Journal of Materials Science: Materials in Electronics*. **30** (2019). https://doi.org/10.1007/s10854-018-006300.

[8] S. Tripathi, Sadanand, P. Lohia, D.K. Dwivedi, Contribution to sustainable and environmental friendly non-toxic CZTS solar cell with an innovative hybrid buffer layer, *Solar Energy*. **204** (2020). https://doi.org/10.1016/j.solener.2020.05.033.

[9] A. Sharmin, M.S. Bashar, S. Tabassum, Z.H. Mahmood, Low cost and sol-gel processed earth abundant cu2znsns4 thin film as an absorber layer for solar cell: Annealing without sulfurization, *International Journal of Thin Film Science and Technology*. **8** (2019). https://doi.org/10.18576/ijtfst/080206.

[10] U.A. Shah, A. Wang, M. Irfan Ullah, M. Ishaq, I.A. Shah, Y. Zeng, M.S. Abbasi, M.A. Umair, U. Farooq, G.X. Liang, K. Sun, A Deep Dive into Cu2ZnSnS4 (CZTS) Solar Cells: A Review of Exploring Roadblocks, Breakthroughs, and Shaping the Future, *Small*. (2024). https://doi.org/10.1002/smll.202310584.

[11] G. Chen, W. Wang, J. Zhang, S. Chen, Z. Huang, R. Jian, Ultra-high sulfurization temperature drives the growth of oxide-derived Cu2ZnSnS4 thin film with very large grain, *Journal of Renewable and Sustainable Energy*. **9** (2017). https://doi.org/10.1063/1.4973716.

[12] C. Santana Maldonado, A. Weir, W.K. Rumbeiha, A comprehensive review of treatments for hydrogen sulfide poisoning: past, present, and future, *Toxicol Mech Methods*. **33** (2023). https://doi.org/10.1080/15376516.2022.2121192.

[13] A.A. Fazri, A.N. Puspita, S. Ningsih, A. Auliya, Electrodeposition of CoNi Bimetallic Catalyst for Ethanol Electrooxidation Application, *Chemistry and Materials*. **2** (2023) 56–60. https://doi.org/10.56425/cma.v2i3.63.

[14] M.A. Rizqi Maulana, Aisyaturridha, Salmah Cholilah, F. Dwi Arista, Bagus Nur Listiyono, Nickel Oxide (NiO) Thin Film Synthesis via Electrodeposition for Methylene Blue Photodegradation, *Chemistry and Materials*. **2** (2023) 61–66. https://doi.org/10.56425/cma.v2i3.62.

[15] G.I. Rofi, M. Paristiowati, The Effect of Electrodeposition Current and Electrolyte Composition on Electrodeposition of Fe-Ni Alloys, *Chemistry and Materials*. **1** (2022) 55–60. https://doi.org/https://doi.org/10.56425/cma.v1i2.27 Original.

[16] Alfian Putra Utama, Afrizal, Electrodeposition of CoNi Cocatalyst to Enhance Ethanol Electrooxidation of Zn-doped Cu2O-Cu Photocatalyst, *Chemistry and Materials*. **2** (2023). https://doi.org/10.56425/cma.v2i1.44.

[17] J. Zhang, S. Yan, S. Zhao, Q. Xu, C. Li, Photocatalytic activity for H 2 evolution of TiO 2 with tuned surface crystalline phase, *Appl Surf Sci*. **280** (2013). https://doi.org/10.1016/j.apsusc.2013.04.153.

[18] V. Madhavi, P. Kondaiah, H. Shaik, G.M. Rao, Phase dependent photocatalytic activity of Ag loaded TiO 2 films under sun light, *Appl Surf Sci*. **364** (2016). https://doi.org/10.1016/j.apsusc.2015.12.133.

[19] S. Jin, X. Wang, X. Wang, M. Ju, S. Shen, W. Liang, Y. Zhao, Z. Feng, H.Y. Playford, R.I. Walton, C. Li, Effect of Phase Junction Structure on the Photocatalytic Performance in Overall Water Splitting: Ga2O3 Photocatalyst as an Example, *Journal of Physical Chemistry C*. **119** (2015). https://doi.org/10.1021/acs.jpcc.5b04092.

[20] C. Zhang, H. Zhang, K. Zhang, X. Li, Q. Leng, C. Hu, Photocatalytic activity of ZnWO4: Band structure, morphology, and surface modification, *ACS Appl Mater Interfaces*. **6** (2014). https://doi.org/10.1021/am503696b.

[21] S. Azmi, O.A. Layachi, M.E. Ouardi, E.M. Khoumri, A. Moujib, A.E. Brouzi, M. Nohair, L. Pezzato, M. Dabala, Growth of Cu2ZnSnS4 thin film absorber layer on transparent conductive oxides and molybdenum substrates by electrodeposition for photovoltaic application, *Optik (Stuttg)*. **250** (2022). https://doi.org/10.1016/j.ijleo.2021.168320.

[22] A. Meng, H. Zhang, B. Huangfu, W. Tian, L. Sheng, Z. Li, S. Tan, Q. Li, Bimetal nickel–cobalt phosphide directly grown on commercial graphite substrate by the one-step electrodeposition as efficient electrocatalytic electrode, *Progress in Natural Science: Materials International*. **30** (2020). https://doi.org/10.1016/j.pnsc.2020.08.003.

[23] L.Y. Su, C.R.M. Grovenor, M.J. Goringe, Fabrication of tbcco films via sequential electrodeposition and co-electrodeposition of thallium-free precursors, *Supercond Sci Technol*. **7** (1994). https://doi.org/10.1088/0953-2048/7/3/008.

[24] A.I.N. Turmiasaputri, Erfan Handoko, S. Budi, The Effect of Temperature and pH on FeCoNi Film Electrodeposition, *Chemistry and Materials*. **1** (2022) 61–65. https://doi.org/10.56425/cma.v1i2.25.

[25] M.G. Sutrisno, N. Fauziyyah, M. Paristiowati, The Effects of Aniline Concentration and Deposition Time on Polyaniline Conductance as Substrate in Fe / Ni Electrodeposition, *Chemistry and Materials*. **1** (2022) 12–17.

[26] A. Agasti, S. Mallick, P. Bhargava, Electrolyte pH dependent controlled growth of co-electrodeposited CZT films for application in CZTS based thin film solar cells, *Journal of Materials Science: Materials in Electronics*. **29** (2018). https://doi.org/10.1007/s10854-017-8350-z.

[27] M. Tanaka, Y. Hirose, Y. Harada, M. Takahashi, Y. Sakata, S. Higashimoto, Fabrication of Cu2ZnSnS4 (CZTS) by co-electrodeposition of Cu-Zn-Sn alloys, and effect of chemical composition of CZTS on their photoelectrochemical water splitting, *Results Chem*. **5** (2023). https://doi.org/10.1016/j.rechem.2023.100900.

[28] A.E. Rakhshani, A. Bumajdad, F. Al-Sagheer, S. Thomas, P.H. Tharayil, One-step electrodeposition of CuZnSn metal alloy precursor film followed by the synthesis of Cu2ZnSnS4and Cu2ZnSnSe4 light absorber films and heterojunction devices, *Int J Electrochem Sci*. **12** (2017). https://doi.org/10.20964/2017.08.22.

[29] J. Henry, K. Mohanraj, G. Sivakumar, Effect of pH-induced on the photosensitivity of non-toxic Cu2ZnSnS4 thin film by chemical bath deposition, *Optik (Stuttg)*. **141** (2017). https://doi.org/10.1016/j.ijleo.2017.03.121.

[30] S.H. Huh, Y.J. Choi, S.H. Kim, J.S. Bae, S.H. Lee, S.H. Yu, Enabling uniform zinc deposition by zwitterion additives in aqueous zinc metal anodes, *J Mater Chem A Mater*. **11** (2023). https://doi.org/10.1039/d3ta01943h.

[31] T. Boiadjieva, M. Monev, A. Tomandl, H. Kronberger, G. Fafilek, Electrochemical studies on Zn deposition and dissolution in sulphate electrolyte, *Journal of Solid-State Electrochemistry*. **13** (2009). https://doi.org/10.1007/s10008-008-0594-3.

[32] M. Farbod, A. Mohammadian, K. Ranjbar, R. Kouhpeymani Asl, Effect of Sintering on the Properties of γ-Brass (Cu5Zn8) Nanoparticles Produced by the Electric Arc Discharge Method and the Thermal Conductivity of γ-Brass Oil-Based Nanofluid, *Metall Mater Trans A Phys Metall Mater Sci*. **47** (2016). https://doi.org/10.1007/s11661-015-3295-4.

[33] H.K. Ng, D. Xiang, A. Suwardi, G. Hu, K. Yang, Y. Zhao, T. Liu, Z. Cao, H. Liu, S. Li, J. Cao, Q. Zhu, Z. Dong, C.K.I. Tan, D. Chi, C.W. Qiu, K. Hippalgaonkar, G. Eda, M. Yang, J. Wu, Improving carrier mobility in two-dimensional semiconductors with rippled materials, *Nat Electron*. **5** (2022). https://doi.org/10.1038/s41928-022-00777-z.

[34] B. Philippa, M. Stolterfoht, P.L. Burn, G. Juška, P. Meredith, R.D. White, A. Pivrikas, The impact of hot charge carrier mobility on photocurrent losses in polymer-based solar cells, *Sci Rep*. **4** (2014). https://doi.org/10.1038/srep05695.

[35] S. Dilger, S. Landsmann, M. Trottmann, S. Pokrant, Carbon containing conductive networks in composite particle-based photoanodes for solar water splitting, *J Mater Chem A Mater*. **4** (2016).https://doi.org/10.1039/c6ta06360h.

[36] C. Qiao, Q. Wu, L. Hao, Y. Wang, X. Sun, Q. Zou, X. An, Native oxide film powered corrosion protection of underlying Pb-free Sn solder substrate, *Corros Sci*. **221** (2023). https://doi.org/10.1016/j.corsci.2023.111359.

[37] K. Kaur, N. Kumar, M. Kumar, Strategic review of interface carrier recombination in earth abundant Cu-Zn-Sn-S-Se solar cells: current challenges and future prospects, *J Mater Chem A Mater*. **5** (2017). https://doi.org/10.1039/C6TA10543B.

[38] J. Xu, Z. Zhao, W. Wei, G. Chang, Z. Xie, W. Guo, D. Liu, D. Qu, H. Tang, J. Li, Tuning the Intrinsic Activity and Electrochemical Surface Area of MoS2 via Tiny Zn Doping: Toward an Efficient Hydrogen Evolution Reaction (HER) Catalyst, *Chemistry - A European Journal*. **27** (2021). https://doi.org/10.1002/chem.202102803.

[39] M. Ali, E. Pervaiz, T. Noor, O. Rabi, R. Zahra, M. Yang, Recent advancements in MOF-based catalysts for applications in electrochemical and photoelectrochemical water splitting: A review, *Int J Energy Res*. **45** (2021). https://doi.org/10.1002/er.5807.

[40] A.P. Murthy, J. Theerthagiri, J. Madhavan, Insights on Tafel Constant in the Analysis of Hydrogen Evolution Reaction, *Journal of Physical Chemistry C*. **122** (2018). https://doi.org/10.1021/acs.jpcc.8b07763.

[41] R. V. Digraskar, S.M. Mali, S.B. Tayade, A. V. Ghule, B.R. Sathe, overall noble metal free Ni and Fe doped Cu 2 ZnSnS 4 (CZTS) bifunctional electrocatalytic systems for enhanced water splitting reactions, *Int J Hydrogen Energy*. **44** (2019). https://doi.org/10.1016/j.ijhydene.2019.02.054.